



Deposited via The University of Sheffield.

White Rose Research Online URL for this paper:

<https://eprints.whiterose.ac.uk/id/eprint/199420/>

Version: Published Version

---

**Article:**

Game, O.S., Thornber, T., Cepero-Mejías, F. et al. (2024) Direct integration of perovskite solar cells with carbon fibre substrates. *Advanced Materials*, 36 (20). e2209950. e2209950. ISSN: 0935-9648

<https://doi.org/10.1002/adma.202209950>

---

**Reuse**

This article is distributed under the terms of the Creative Commons Attribution (CC BY) licence. This licence allows you to distribute, remix, tweak, and build upon the work, even commercially, as long as you credit the authors for the original work. More information and the full terms of the licence here:

<https://creativecommons.org/licenses/>

**Takedown**

If you consider content in White Rose Research Online to be in breach of UK law, please notify us by emailing [eprints@whiterose.ac.uk](mailto:eprints@whiterose.ac.uk) including the URL of the record and the reason for the withdrawal request.

# Direct Integration of Perovskite Solar Cells with Carbon Fiber Substrates

Onkar S. Game, Timothy Thornber, Fernando Cepero-Mejías, Luis C. Infante-Ortega, Mustafa Togay, Elena J. Cassella, Rachel C. Kilbride, Robert H. Gordon, Nic Mullin, Rachael C. Greenhalgh, Patrick J. M. Isherwood, J. Michael Walls, J. Patrick A. Fairclough, and David G. Lidzey\*

**Integrating photovoltaic devices onto the surface of carbon-fiber-reinforced polymer substrates should create materials with high mechanical strength that are also able to generate electrical power. Such devices are anticipated to find ready applications as structural, energy-harvesting systems in both the automotive and aeronautical sectors. Here, the fabrication of triple-cation perovskite n–i–p solar cells onto the surface of planarized carbon-fiber-reinforced polymer substrates is demonstrated, with devices utilizing a transparent top ITO contact. These devices also contain a “wrinkled” SiO<sub>2</sub> interlayer placed between the device and substrate that alleviates thermally induced cracking of the bottom ITO layer. Devices are found to have a maximum stabilized power conversion efficiency of 14.5% and a specific power (power per weight) of 21.4 W g<sup>-1</sup> (without encapsulation), making them highly suitable for mobile power applications.**

single-junction devices (25.7%) now approaching that of top-performing silicon solar cells.<sup>[1]</sup> The outstanding optoelectronic properties, high lab-scale efficiencies, and facile, low-cost solution processability make perovskite PV an ideal system for integration with novel substrate materials that have thermal processing limitations.<sup>[2]</sup> This allows perovskite solar cells (PSCs) to be deposited onto flexible polymer substrates, with other work demonstrating devices that are transparent or have high performance under diffuse or low light conditions.<sup>[3,4]</sup> These advantages may allow PSCs to operate in niche applications where crystalline silicon is poorly suited. Indeed, PSCs have been integrated with a variety of materials, including transparent polymers—namely

poly(ethylene terephthalate)<sup>[5]</sup> (PET) and poly(ethylene naphthalate)<sup>[3]</sup> (PEN), metal foils such as titanium<sup>[6,7]</sup> and copper,<sup>[8]</sup> titanium<sup>[9]</sup> and steel,<sup>[10]</sup> metal wires<sup>[11,12]</sup> and fibers;<sup>[13,14]</sup> and even paper.<sup>[15,16]</sup> For readers interested in fiber based PSCs, we highlight a recent review.<sup>[17]</sup> Such integration of PSCs with novel substrate materials opens a broad range of possible

## 1. Introduction

Organic–inorganic hybrid perovskite materials have generated substantial interest within the photovoltaic (PV) research community, with the record power conversion efficiency (PCE) of

O. S. Game<sup>[+]</sup>, T. Thornber, E. J. Cassella, R. C. Kilbride<sup>[++]</sup>, R. H. Gordon, N. Mullin, D. G. Lidzey  
Department of Physics & Astronomy  
University of Sheffield  
Hicks Building, Hounsfield Road, Sheffield S3 7RH, UK  
E-mail: d.g.lidzey@sheffield.ac.uk

F. Cepero-Mejías, J. P. A. Fairclough  
Department of Mechanical Engineering  
University of Sheffield  
Sir Frederick Mappin Building, Mappin Street, Sheffield S1 3JD, UK  
L. C. Infante-Ortega, M. Togay, R. C. Greenhalgh, P. J. M. Isherwood,  
J. M. Walls  
CREST  
Wolfson School of Mechanical  
Electrical and Manufacturing Engineering  
Loughborough University  
Loughborough, Leicestershire LE11 3TU, UK

 The ORCID identification number(s) for the author(s) of this article can be found under <https://doi.org/10.1002/adma.202209950>

<sup>[+]</sup>Present address: Department of Physics, Indian Institute of Technology (IIT) – Indore, Khandwa Road, Simrol, Indore, Madhya Pradesh 453552, India

<sup>[++]</sup>Present address: Department of Chemistry, University of Sheffield, Dainton Building, Brook Hill, Sheffield S3 7HF, UK

© 2023 The Authors. Advanced Materials published by Wiley-VCH GmbH. This is an open access article under the terms of the Creative Commons Attribution License, which permits use, distribution and reproduction in any medium, provided the original work is properly cited.

DOI: 10.1002/adma.202209950

applications ranging from portable or wearable consumer electronics to power sources for the “internet of things”.<sup>[18–20]</sup>

One particular emerging application of PSC-based technologies is in decentralized solar power generation, where high power-per-weight (or specific power) is critical. This is most important in the automotive and aerospace industries, building-integrated PV and military applications. Previous work by Kaltenbrunner et al. demonstrated that the specific power of PSCs outperforms that of all other PV materials while rivalling those of other power generation technologies.<sup>[21]</sup> Here, ultralightweight, 3  $\mu\text{m}$ -thick PSCs were fabricated on a PET foil, with devices having a PCE of 12% and a specific power of up to 23  $\text{W g}^{-1}$ . Such devices were shown to be capable of powering a direct-current motor for a model aeroplane when connected to an  $8 \times 8$  PSC array. Kang et al. have also created flexible PSCs having a specific power of 29.4  $\text{W g}^{-1}$  with devices being light enough to rest on the surface of soap bubbles.<sup>[22]</sup> More recently, Wu et al. have demonstrated ultrathin PSCs fabricated on parylene substrates using a flip-over transfer technique, with devices demonstrated to have a PCE of up to 20.2% with a record specific power of 30.3  $\text{W g}^{-1}$ .<sup>[23]</sup>

The application of PSCs for portable power applications therefore represents an extremely attractive prospect, with one possible application route being the lamination of flexible PSC devices onto curved surfaces such as the envelope of a dirigible, the fuselage of an aircraft or the monocoque of an automobile.<sup>[21]</sup> We believe, however, that this approach has some drawbacks. In particular, the weight of the substrate and associated adhesives is expected to reduce the specific power of the resultant device, with the potential delamination of the device from the surface of interest representing a possible failure mechanism. Furthermore, while it is possible to “wrap” a 2D flexible PV device over a surface that curves in one direction (e.g., a cylinder), it is not possible to wrap a flexible device over a complex surface that curves in two directions (e.g., a sphere); a limitation that restricts the surfaces over which such an approach can be applied.<sup>[24]</sup> Indeed, PSC devices fabricated on flexible substrates can also have a limited bend-radius;<sup>[25]</sup> a feature that could limit the curvature of the surface on which they can be fixed. Finally, we note that the performance metrics of flexible PSCs currently lag behind those of rigid cells with such devices prone to mechanical fracture due to repeated flexing.<sup>[26]</sup>

An alternate approach to utilizing PSCs for mobile power applications that we explore here involves directly coating such devices onto a surface of choice. Here, a key material of interest for mobile power applications are carbon-fiber-reinforced polymer (CFRP) composites. These materials are widely used in the automotive (e.g., high-performance race cars) and aerospace (e.g., aircraft fuselages) industries as they combine high strength and elastic modulus compared to metallic materials or other structural polymers.<sup>[27,28]</sup> Here, the combination of PSCs with CFRP composites creates materials having a unique balance of high power-per-weight and high strength-per-weight, realizing a class of structural materials that also act as a power source. Critically, the ability to process PSCs from solution using techniques such as spray coating allows them to be deposited over curved surfaces.<sup>[29]</sup> PSC devices on CFRP composites could be readily employed in unmanned aerial vehicles (UAVs) and high-altitude pseudo-satellites (HAPSs), where there are stringent weight limi-

tations and finite fixed wingspans.<sup>[30]</sup> Indeed, it has been demonstrated that by integrating solar cells over curved surfaces, devices can be realized having a power output exceeding that of planar cells occupying an equivalent area.<sup>[31,32]</sup> We note, however, that CFRP composites often have a high level of surface roughness that is much greater than the polished glass surfaces on which PSCs are most often deposited, and planarizing such surfaces is expected to be a key challenge.

In this paper, we directly fabricate n-i-p architecture “triple-cation” (TC) based PSCs (ITO/SnO<sub>2</sub>/TC-perovskite/spiro-OMeTAD/Au (0.8 nm)/ITO) in substrate configuration onto epoxy-planarized CFRP composite substrates, with devices illuminated through a transparent top indium tin oxide (ITO) contact. A key challenge we address is the preparation of the CFRP surface. We show that the roughness of such a surface can be substantially reduced to a root-mean-squared (RMS) roughness of 29 nm by using a commercial epoxy-based mesh material. However, the differing thermal expansion coefficients of the ITO charge-extracting layer and the CFRP substrate leads to severe cracking during the thermal annealing necessary to process the TC-perovskite. We show that this problem can be overcome via the use of an intermediate “wrinkled” SiO<sub>2</sub> film placed between the ITO and the CFRP surface, which prevents cracking of the ITO during annealing. Using this approach, we realize devices having PCEs up to 14.4% and stabilized PCEs of 14.5%. The use of Au (0.8 nm)/ITO as a transparent top contact results in devices having promising stability, with control (glass-substrate) PSCs having dark-storage lifetimes in excess of 1 month.

## 2. Results

### 2.1. Preparation of the CFRP Substrate

Samples were fabricated from unidirectional XC130 “pre-preg” (Easy Composites Ltd, Stoke on Trent, UK). This material is typical of those used in the automotive and aerospace industries and was selected due to its high carbon fiber-content and strength after curing. XC130 is composed of unidirectional carbon fiber pre-impregnated with a bisphenol-A-based epoxy resin. A cleaned, scratch free, smooth glass substrate was prepared with a release film and three XC130 20  $\times$  20 cm sheets. A breather fabric was then placed on top of the CFRP pre-preg sheets and the assembly placed inside an air-tight bag before a vacuum was applied. The pre-preg-glass assembly was then placed inside an autoclave that was pressurized to 6 bar and heated at a rate of 2  $^{\circ}\text{C min}^{-1}$  to 100  $^{\circ}\text{C}$ . The assembly was then held at 100  $^{\circ}\text{C}$  for 4 h to cure. Pressure and temperature were then slowly reduced at 0.2 bar  $\text{min}^{-1}$  and 2  $^{\circ}\text{C min}^{-1}$  to return the assembly to atmospheric conditions. The resultant sample had a thickness of 0.9 mm and an areal mass of 1050  $\text{g m}^{-2}$ . To prepare samples for device fabrication, the 20  $\times$  20 cm sheets were waterjet cut (ProtoMax) into 19  $\times$  15 mm sections.

**Figure 1a** shows an image of a CFRP substrate, with **Figure 1b** showing a surface topograph of its surface recorded using a Dektak surface profilometer system. It was found, as expected, that such surfaces were relatively rough with an RMS roughness of 35 nm over a 2  $\times$  2 mm area, and peak height features of up to 1.2  $\mu\text{m}$ ; values likely problematic for the direct integration of PSC devices. Here, a series of carbon fibers can be seen that are close

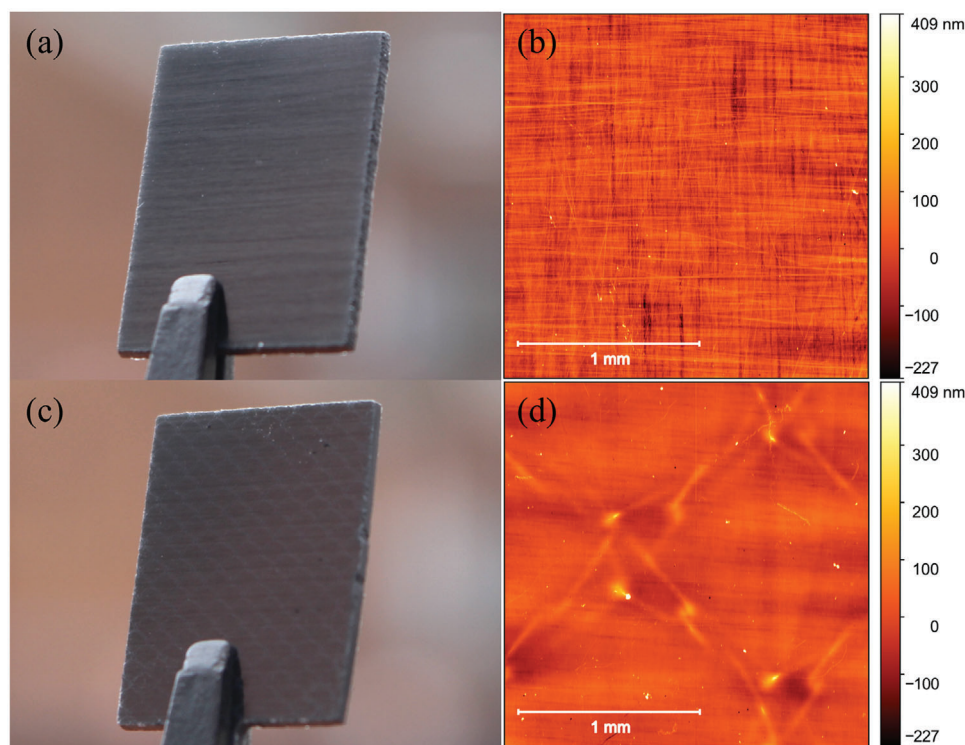


**Figure 1.** a,c) Photographs of unplanarized (a) and planarized (C) CFRP composite substrates. b,d) Corresponding surface topography maps of unplanarized (b) and planarized (CFRP composite substrates).

to the surface and are not entirely encapsulated by the epoxy matrix. Such carbon fibers render the CFRP electrically conductive, with a resistance of  $20 \Omega$  typically measured between points 1 cm apart on the surface. While such conductivity could be potentially helpful for future applications, here it was found to generate electrical pathways that resulted in short-circuited devices. To overcome such issues, the surface was coated by a planarization layer that both reduced the roughness of the CFRP and rendered its surface electrically insulating.

The planarization layer was based on an XA120 epoxy-resin adhesive film (Easy Composites) that is generally utilized to bond honeycomb aluminium, Nomex or foam structures to composite parts. This material was placed on the surface of the CFRP next to the glass mould surface. XA120 was used due to its excellent adhesion to the XC130 CFRP and its ability to reduce surface roughness substantially. Figure 1c shows an image of a CFRP substrate with an XA120 epoxy laminate that was obtained by cutting individual substrates via a waterjet cutter, with a surface topograph of the same surface shown in Figure 1d. The planarization layer was found to reduce the RMS surface roughness to 29 nm over  $2 \times 2$  mm, with maximum peak heights being  $\approx 400$  nm. This compares with a typical RMS roughness of 13 nm for a quartz-coated glass substrate over a similar length scale. A honeycomb motif having a height of  $\approx 350$  nm can be seen in the topography map. This structure originates from the supporting mesh within the epoxy planarization layer. As the core-mesh structure has a low aspect ratio, we found that subsequent coatings formed a completely conformal layer over the surface that made them suitable substrates for device fabrication.

## 2.2. Deposition of the ITO Bottom Contact

PSC device fabrication proceeded with an ITO bottom contact deposition onto the planarized CFRP. To ensure an effective, strong bond was formed between the ITO and the CFRP, the surface was first treated using a commercially available primer layer (Plastic-coat Plastic Primer) that was spray-cast onto the CFRP surface. ITO was then deposited onto the primed planarization layer via RF sputtering at a deposition power of 155 W from a 4" diameter ITO target in a vacuum chamber through which argon gas flowed at 7 SCCM. In all cases, ITO films were not heated during or after their deposition. The bottom ITO films deposited on the CFRP substrate had a typical thickness of 200 nm and sheet resistance of  $20 \Omega/\square$ . The transmission of a typical ITO film deposited on glass is shown in Figure 2a, where the film has an optical transmission of 86.1% at 480 nm. While it is not possible to directly measure the optical transmission of ITO films deposited onto CFRP substrates (as they are completely opaque), we have characterized their optical properties by measuring their angular-dependent optical reflectivity. Typical reflectivity data for ITO films deposited by sputtering on both glass and CFRP substrates is shown in Figure S1 (Supporting Information). Here, we find that the optical-reflectivity of the ITO deposited on each type of substrate is very similar, with any differences likely resulting from the underlying CFRP/ITO interface.

Atomic force microscopy (AFM) measurements (see Figure S2, Supporting Information) indicated that the ITO deposited onto the CFRP/primer surface was relatively smooth, having an RMS roughness of 15 nm over a length scale of

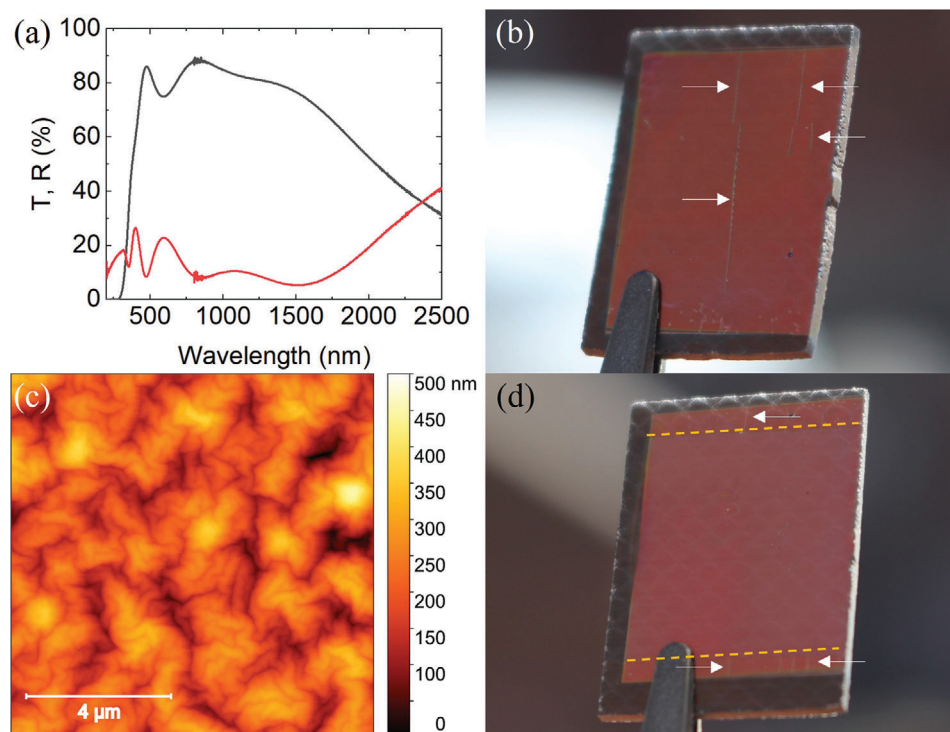


**Figure 2.** a) Optical transmission ( $T$ ) (black) and reflectance ( $R$ ) (red) for the bottom ITO electrode when fabricated on glass. b) Photograph of an ITO-coated CFRP-planarized substrate heated to 100 °C in the absence of the crack-preventing  $\text{SiO}_2$  layer. Here, cracks (marked by white arrows) in the ITO layer can be clearly seen. c) AFM image of the surface of a CFRP-planarized substrate upon which  $\text{SiO}_2$  has been deposited via e-beam evaporation. d) Photograph of an ITO coated CFRP-planarized substrate incorporating the crack-prevention layer, with the whole structure subsequently heated to 100 °C. Note that cracks are visible near the edges of the ITO, but these are completely arrested at the  $\text{SiO}_2$  boundary (marked by yellow dotted lines).

$10 \times 10 \mu\text{m}$ . Despite this promising finding, we found that such multilayer structures were highly unstable when thermally annealed at the temperatures typically used to process materials used in perovskite solar cells. Indeed, significant surface cracking became evident after an ITO covered CFRP substrate had been heated to 100 °C and then cooled to room temperature (see Figure 2b). This resulted in the failure of all devices fabricated onto such CFRP surfaces, as the cracks generated electrical short circuits between the ITO and the PSC top contact. We suspect that the cracking of the ITO resulted from the fact that the coefficient of thermal expansion (CTE) of ITO is an order of magnitude lower than that measured (see Table S1, Supporting Information) for our planarized CFRP (being  $7.2 \times 10^{-6} \text{ K}^{-1}$  and  $7.9 \times 10^{-5} \text{ K}^{-1}$  respectively).<sup>[33]</sup> As a result of this mismatch, the difference in expansion between the substrate and ITO during thermal annealing resulted in the generation and long-range propagation of cracks in the ITO. Such cracks apparently do not “heal” when the substrate is cooled; we suspect that internal tensile stress in the ITO film causes the edges of the cracks to curl away from the surface.

To alleviate this issue, we have incorporated a “crack-prevention” layer between the ITO contact and the planarized CFRP. This approach was inspired by previous work in which ITO was deposited by DC sputtering onto an optically curable epoxy that underwent “wrinkling” and increased both the optical reflectance and flexibility of the ITO film.<sup>[34]</sup> We note that similar wrinkled poly(vinylidene fluoride-hexafluoropropylene)

substrates have previously been shown to improve the ductility of a brittle poly(selenophene-*alt*-3,6-dithiophene-2-yl-2,5-bis-(2-octyldodecyl)-2,5-dihydro-pyrrolo[3,4-*c*]pyrrole-1,4-dione) thin film via a stress-reduction mechanism.<sup>[35]</sup> In our experiments, the crack-prevention layer was based on a 150 nm-thick layer of  $\text{SiO}_2$  deposited via e-beam evaporation onto the primed CFRP substrate. As seen in the AFM image shown in Figure 2c, this layer has a densely wrinkled structure, with such wrinkles having lateral dimensions of up to  $2.5 \mu\text{m}$  with a height of up to 450 nm. The wrinkled structure is created by the combination of thermal radiation that is generated by the e-beam source as it heats the  $\text{SiO}_2$  target and the kinetic energy of the evaporated material. We suspect that this process provides sufficient energy to cause localized heating of the primer layer and planarization epoxy to cause it to partially soften and expand during the  $\text{SiO}_2$  deposition. On cooling, these layers contract, causing the dense, non-compressible  $\text{SiO}_2$  layer to adopt a highly crumpled structure, as has been demonstrated by depositing metallic films using an e-beam on poly(dimethylsiloxane) (PDMS).<sup>[36]</sup>

An ITO layer was then deposited onto the wrinkled  $\text{SiO}_2$  layer via RF sputtering, forming a near conformal coating. Our experiments demonstrate that such “wrinkled” structures do not form when ITO is directly deposited on the surface of the planarized CFRP as the sputtering process does not appear to generate sufficient heat to soften the surface layer (see Figure S2, Supporting Information). AFM measurements (see Figure S3, Supporting Information) indicate the surface roughness of the

wrinkled ITO is rougher than that of ITO deposited on a polished glass surface (RMS roughness being 27 and 12 nm, respectively, over a scan area of  $5 \times 5 \mu\text{m}$ ). We believe that such wrinkles are not sufficient to cause device failure—indeed, similar structures have been used to enhance light management in thin-film optical devices by—for example—preventing optical waveguiding in organic light emitting diodes and improving light outcoupling.<sup>[37]</sup> Importantly the ITO layer is strongly bonded to the wrinkled  $\text{SiO}_2$ ; this has been confirmed by sticking and then removing an adhesive tape to the surface, performing a so-called “peel test”. Here it was found that the removal of the adhesive tape did not remove or delaminate the ITO layer, indicating that it is strongly attached to the  $\text{SiO}_2$  surface.

We have found that such a wrinkled structure effectively “protects” the ITO during subsequent thermal annealing and cooling processes. Figure 2d shows an image of a  $\text{SiO}_2$ -ITO layer on planarized CFRP that has been thermally annealed at  $100^\circ\text{C}$  before being allowed to cool. Here it can be seen that the ITO remains uncracked, making it a suitable substrate for PSC device deposition. Indeed, we find that if a surface is partially coated using such a “protective” silica layer, then cracks form in the ITO in the unprotected regions upon heating and cooling, however such cracks do not propagate into the protected region (see Figure S4, Supporting Information).

To explore the crack prevention mechanism, we first recorded the CTE of the surface of CFRP substrates both with and without the  $\text{SiO}_2$  layer (see Tables S1 and S2 for raw data, Figures S5 and S6 for experimental set up, Supporting Information for exact methodology). Here, measurements were made along and across the unidirectional carbon fiber axis, as any expansion could reasonably be assumed to be anisotropic. We found that the CTE for samples without the  $\text{SiO}_2$  interlayer measured along and across the fiber axis were  $<1.0 \times 10^{-6}$  and  $7.9 \times 10^{-5} \text{ K}^{-1}$ , respectively. On addition of the  $\text{SiO}_2$  layer, the CTE of the surface layer was largely unchanged, indicating that the wrinkled layer does not modify the degree to which the surface layer expands when heated. Notably, however, the significant anisotropy measured in the CTE explains our observation that cracks in the ITO only develop parallel to the fiber axis, as can be seen in Figure 2b. We have also characterized the surface structure of CFRP substrates with and without the wrinkled- $\text{SiO}_2$  and ITO layers as a function of temperature up to  $150^\circ\text{C}$ . Here, we identify only fairly small changes in the roughness of the wrinkled surface as a function of temperature (see Figures S7 and S8, Supporting Information). We conclude therefore that such wrinkled layers most likely prevent cracking by: 1) creating a roughened surface to which ITO bonds very securely and 2) by preventing the long-range propagation of cracks.

For completeness, we have also investigated the degree to which the wrinkled layer confers additional mechanical protection to the ITO. Here, we carried out 4-point bend tests on ITO-covered CFRP-planarized substrates (having dimensions  $100 \times 25 \text{ mm}$ ) either with or without a wrinkled  $\text{SiO}_2$  protection layer. Details of the experimental set up are shown in Figures S9 and S10 (Supporting Information). During these bending tests, the ITO resistance was measured as a function of roll displacement. Here, we found that ITO resistance remained constant until the center rolls were displaced by  $\approx 3.5 \text{ mm}$ . This level of bend corresponded to an apex displacement of  $\approx 4.6 \text{ mm}$ , and a strain

of 0.45%, as calculated via finite element analysis. Beyond this point, the samples without the  $\text{SiO}_2$  layer underwent a dramatic increase in resistance as a function of deflection. However, the samples incorporating the  $\text{SiO}_2$  layer underwent a more modest, linear increase in resistance (see Figure S11, Supporting Information). We suspect that the crack-prevention layer reduces damage to the ITO at any given strain due to improved adhesion as a result of higher surface roughness that provides a good key for the ITO. We note that during these tests, the force required to achieve a strain of 0.45% was calculated to be in excess of 100 N; this force is well beyond that which soda-lime glass substrates of the same thickness would undergo complete failure.<sup>[38,39]</sup>

### 2.3. Device Fabrication and Testing

We have used the structures described above as the substrates for PSC devices. A typical device stack is shown schematically in Figure 3a. Devices were fabricated on planarized CFRP substrates together with control devices on standard ITO/glass substrates. In all cases, devices utilized an electron extraction layer based on a colloidal  $\text{SnO}_2$  nanoparticle dispersion that was spin-cast onto the ITO and then thermally annealed at  $100^\circ\text{C}$  for 30 min before being treated via exposure to a UV-generated ozone source for 20 min. Following this, a spin-cast TC-perovskite was deposited onto the  $\text{SnO}_2$  layer from a DMF/DMSO solution and then quenched during the spin-coating cycle using a chlorobenzene antisolvent to initiate nucleation of the perovskite grains. Following a thermal anneal at  $100^\circ\text{C}$  for 20 min, a perovskite film was formed, having an optical bandgap of 1.61 eV, or 770 nm (see Figure S12, Supporting Information). Following this, a hole-extraction layer of doped spiro-OMeTAD was spin-cast onto the perovskite surface. Full experimental details of materials and processing techniques can be found in previous publications and Supporting Information.<sup>[40,41]</sup>

Importantly, as the CFRP substrate is completely opaque, it was necessary to design the device such that light could enter the device through a transparent top contact. This was achieved by sputter coating a film of ITO onto the top spiro-OMeTAD. This was done via a two-step deposition process<sup>[42]</sup> in which a 30 nm-thick ITO “buffer” layer was first sputtered at 40 W, followed by the deposition at 200 W of a thicker (80 nm) “bulk” layer. The use of a buffer layer deposited at a lower magnetron power was found to reduce damage to the spiro-OMeTAD hole-transport layer due to reduced exposure to the magnetron plasma. The two-step deposition process used 10 SCCM of argon for both stages, creating a film with a sheet resistance of  $42 \Omega/\square$  and an optical transmission of 91.2% at 529 nm (see Figure 3b). The ITO contact was deposited through a shadow mask, creating a series of pixels, each having an active area of  $6 \text{ mm}^2$ . To further protect the spiro-OMeTAD hole-transport layer, we found that it was necessary to insert a thin (0.8 nm) gold film (deposited by thermal evaporation) between the ITO and the spiro-OMeTAD hole-transport layer. Without this layer, we found that the device *JV* curves typically had an “s-shape”, indicating an inefficient extraction of carriers (see Figure S13, Supporting Information). Here, we suspect that the plasma utilized during the ITO sputter deposition partially degraded the surface of the spiro-OMeTAD and reduced its ability to conduct charge, with the thin gold layer both

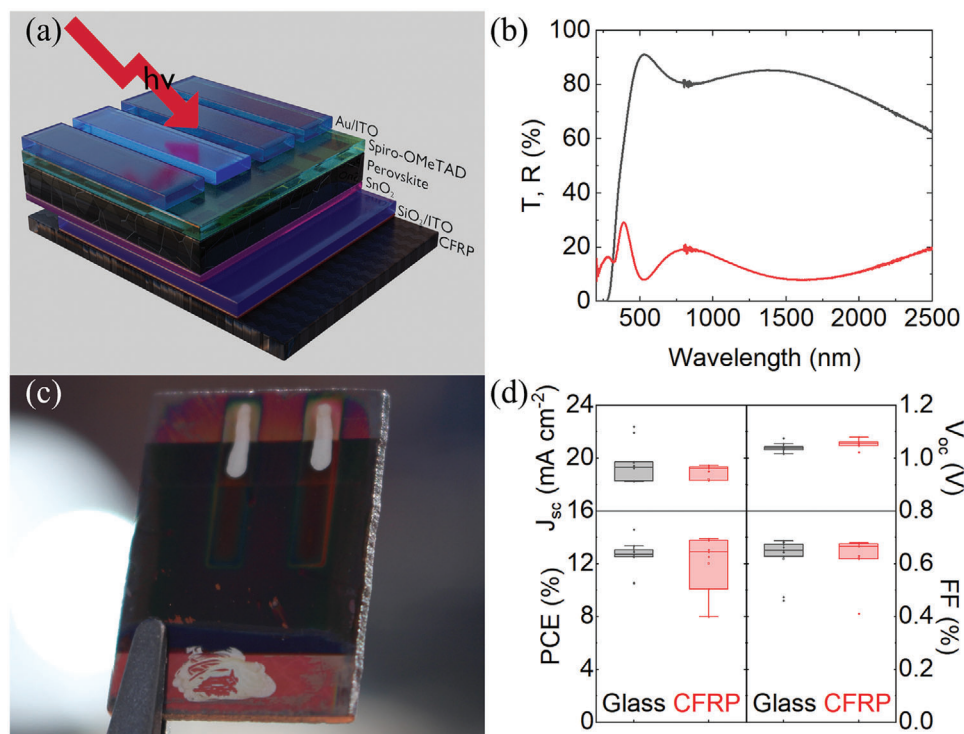


**Figure 3.** a) Schematic of our typical device structure, with an arrow to indicate direction of illumination. b) Optical transmission ( $T$ ) (black) and reflectance ( $R$ ) (red) of the top ITO electrode when deposited on glass. c) Photograph of PSC devices on CFRP composite. Note that the light-gray material visible on each device pixel and the bus bar is silver loaded paste that was used to improve electrical contact to the device. d) Box-plot summary of key device performance metrics derived from reverse  $JV$  sweeps of control devices fabricated on glass together with those on CFRP.

acting as a protection layer by attenuating the passage of ionizing species into the spiro-OMeTAD and also enhancing charge extraction from the spiro-OMeTAD into the ITO. Finally, to improve device efficiency, an anti-reflection layer consisting of 100 nm of LiF was deposited onto the ITO surface via thermal evaporation.

Figure 3c shows an image of a fully fabricated device on a CFRP substrate. Electrical contact was made to each device using a semiconductor probe station, with efficiency measurements performed through an aperture mask (area 2.385 mm<sup>2</sup>) placed onto the surface of the substrate (see Figure S14, Supporting Information). Figure 3d shows box plots of the key device metrics (PCE,  $J_{sc}$ ,  $V_{oc}$  and FF), with data recorded from 8 independent devices containing 16 pixels in total. Here, it can be seen that we record a mean average device PCE of 12.0% with a typical device yield of  $\approx 40\%$ . We attribute the relatively low device yield to the fact that the ITO/CFRP surface is rougher than commercially available ITO coated glass substrates. Such roughness can result in device failure through the generation of electrical short-circuits. We believe that further optimization of the CFRP fabrication and planarization processes will lead to surfaces having reduced roughness and thus improved device yield.

Figure 3d also shows device performance metrics for a series of control devices fabricated onto an ITO/glass substrate. Here, the device stack is identical to that shown in Figure 3a except for the CFRP substrate (i.e., incorporating a transparent ITO top contact). For the sake of fair comparison, control devices were illuminated through the top ITO contact using an aperture mask in a similar way to that used to study devices on the opaque CFRP

substrates. Here, we find that the mean average device efficiency was  $\approx 12.5\%$ , with the performance of the control devices closely matching that of the devices fabricated on CFRP. We attribute the relatively low PCE of the control devices on a glass substrate to the fact that they are illuminated through the top of the device, with light passing through the ITO, gold (0.8 nm) and spiro-OMeTAD layers before reaching the active perovskite layer. This results in significant parasitic absorption by the UV/blue absorbing spiro-OMeTAD layer (bandgap of 2.70–2.98 eV<sup>[43,44]</sup>). This is in contrast to a typical  $n-i-p$  stack that is illuminated through its substrate. In such devices, it is only necessary for light to pass through a thin (30 nm), wide-bandgap (3.6–4.2 eV<sup>[40]</sup>) SnO<sub>2</sub> layer before absorption by the perovskite, with the SnO<sub>2</sub> layer resulting in negligible optical losses. To confirm that our glass control devices were fully optimized, we first recorded  $JV$  curves in which devices were instead illuminated through the glass substrate. Here, we determined PCE values of up to 16.2%; a result that confirms the effect of parasitic absorption within the spiro-OMeTAD (see Figure S15, Supporting Information). We then fabricated identical control devices in which the top Au (0.8 nm)/ITO layer was replaced by a conventional thick (80 nm) Au electrode. Devices were then illuminated through the bottom ITO/SnO<sub>2</sub> contact. Figure S15 (Supporting Information) plots typical  $JV$  curves, where it can be seen that best performing devices had a PCE of 20.2%; a value commensurate with this  $n-i-p$  device architecture. We therefore conclude that the reduced efficiency of devices fabricated on CFRP substrates results from optical absorption in the spiro-OMeTAD layer and the lack of a back-reflector to recycle light not absorbed

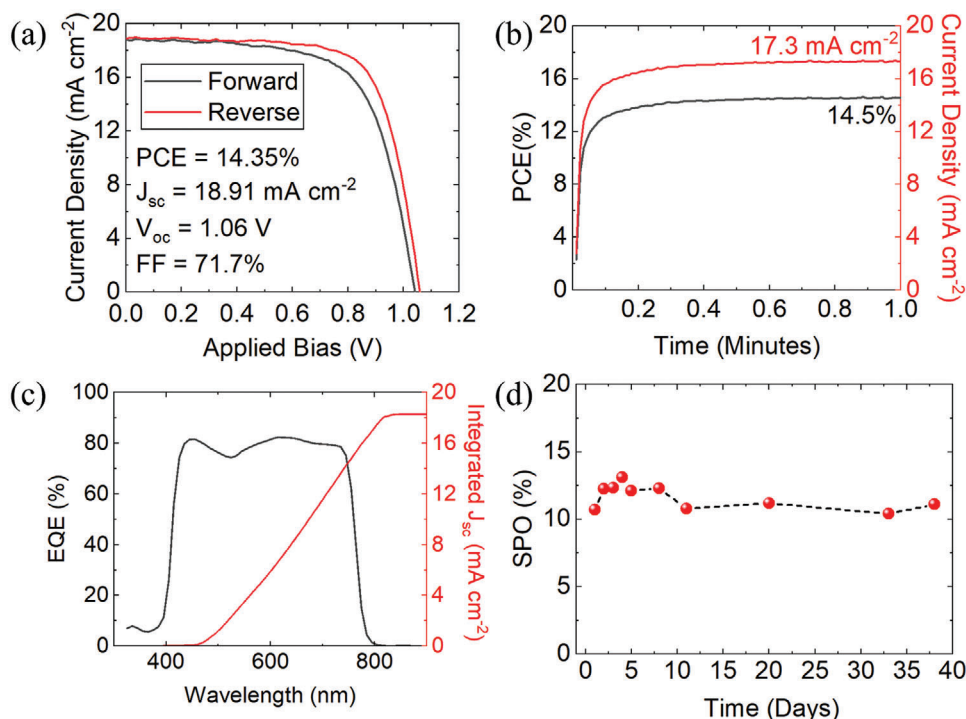


**Figure 4.** a) *JV* data for the champion CFRP-based device, with metrics derived from the reverse sweep. b) Details the stabilized power output of the same device held at close to the maximum power point voltage for 60 s. c) EQE spectrum of a typical CFRP-based device. d) Stabilized power output of glass control devices as a function of storage time in air.

in the perovskite on its first optical pass, together with a relatively higher sheet resistance of the ITO top contact in comparison with that of a thick gold electrode.

For completeness, **Figure 4a** plots a *JV* curve under AM1.5 irradiation of the champion CFRP device. Here, the device had a  $J_{sc}$  of  $18.91 \text{ mA cm}^{-2}$ , a  $V_{oc}$  of  $1.06 \text{ V}$ , an FF of  $71.7\%$  and a PCE of  $14.35\%$ . A stabilized power output of  $14.5\%$  was recorded for this device when held under illumination near the maximum power point voltage, as shown in **Figure 4b**. **Figure 4c** shows a typical external quantum efficiency (EQE) spectrum of a device on a CFRP substrate. Here we extract an integrated  $J_{sc}$  value of  $18.3 \text{ mA cm}^{-2}$ ; a value in agreement with the short circuit current determined from the solar simulator measurements. Note that due to parasitic absorption by the spiro-OMeTAD HTL, we see a drop-off in the EQE response between  $300\text{--}400 \text{ nm}$ . The effect of the spiro-OMeTAD absorption is illustrated in **Figure S16** (Supporting Information), where we plot an EQE measurement of a glass control device illuminated through the glass substrate. Here, a UV/blue EQE response is evident as the incident light no longer passes through a spiro-OMeTAD layer.

We have also made a preliminary assessment of the operational stability of the Au( $0.8 \text{ nm}$ )/ITO top electrodes using dark-storage tests, with unencapsulated devices fabricated on glass/ITO electrodes stored in  $30\% \text{ RH}$  air as per ISOS-D-1 requirements.<sup>[45]</sup> Here, such devices were illuminated through the top electrode during testing, with such measurements providing some measure of the stability of this transparent contact. As shown in **Figure 4d**, we find that devices retain  $85\%$  of their peak efficiency during a period of over 35 days. Here, we ascribe

the promising stability to the TC perovskite formulation<sup>[46]</sup> together with the use of an ITO top contact. We note that other approaches to the development of semi-transparent top-contact electrodes based on ultrathin metallic films typically suffer from reduced stability resulting from oxidation or reactions with I ions that diffuse out of the perovskite.<sup>[47–49]</sup> Such reactions do not occur with transparent conductive oxide materials such as ITO, with our selection of materials, therefore, conferring a high degree of intrinsic stability to the device. Indeed, our preliminary findings also suggest that devices fabricated onto CFRP can show a promising level of dark-storage stability (see **Figure S17**, Supporting Information).

### 3. Discussion

We have demonstrated the integration of PSC devices onto planarized carbon fiber substrates, with devices having a similar PCE to control devices fabricated on conventional glass substrates. Although we have used spin-coating to deposit the solution-processable device layers (np-SnO<sub>2</sub> electron-transport layer, TC perovskite precursor, and spiro-OMeTAD hole-transport layer), we note that such layers can be deposited via spray-coating, allowing devices to be created over complex, curved substrates.<sup>[29]</sup>

Our devices are fabricated directly onto a surface that could have a significant second function—e.g., acting as the wing of an aircraft or the roof of a car. To estimate the specific power of our devices, we simply consider the masses of the layers that we have deposited. In our calculation of the areal mass of each

layer, we use its known thicknesses and reported density (see Table S3, Supporting Information, for exact methodology). Using this approach, we find the mass per unit area of our complete PSC devices to be  $\approx 6.78 \text{ g m}^{-2}$ , indicating a specific power of  $\approx 21.4 \text{ W g}^{-1}$ . This value compares favorably with *a*-Si cells<sup>[50]</sup> that have a maximum reported specific power of  $8.31 \text{ W g}^{-1}$  but is, however smaller than the specific power of PSC devices fabricated onto ultrathin flexible PEN ( $29.4 \text{ W g}^{-1}$ )<sup>[22]</sup> or ultrathin flexible parylene-C ( $30.3 \text{ W g}^{-1}$ ).<sup>[23]</sup> We note however that the fabrication of PSC devices onto ultrathin substrates will also require an adhesive layer to attach them to a surface of interest, thereby reducing their effective specific power. Furthermore, as such devices are illuminated through the substrate, the application of adhesives might damage the semiconductor layers, necessitating the use of a back encapsulant layer, with this layer also reducing effective specific power. Finally, as noted above, wrapping of complex shapes via lamination is likely to introduce unwanted pleats into the PSC device.<sup>[24]</sup>

We note that our estimate of specific power ignores the mass of any encapsulation material, with encapsulation being critical for “real-world” applications. Typically, we encapsulate regular devices using a glass coverslip and a UV-cured epoxy; however, this would account for over 98% of the total device mass and would reduce device specific power to just  $0.4 \text{ W g}^{-1}$ . To enhance the specific power of our devices, it will clearly be necessary to develop ultralow mass encapsulation layers, with such layers likely being deposited via a combination of vapor deposition and spray-coating, allowing them to also cover curved surfaces. If we assume the thickness of the encapsulation layers could be reduced to  $\approx 3 \mu\text{m}$  (e.g., composed of an evaporated metal oxide), then we might expect a specific power of  $\approx 5.4 \text{ W g}^{-1}$ . If devices were instead encapsulated using a  $1 \mu\text{m}$ -thick solution-processed polymeric film (such as polyurethane),<sup>[21]</sup> then we estimate a specific power of  $\approx 18.2 \text{ W g}^{-1}$  should be possible. We note that our devices are designed to be rigid rather than flexible; therefore, any polymeric material used would not require a great deal of flexibility. This would allow the utilization of materials having a higher crosslink density and thus superior oxygen and moisture barrier properties.<sup>[51]</sup> Such devices would clearly represent an important step toward the development of practical power sources for mobile automotive and aerospace applications.

#### 4. Conclusion

We have outlined an approach to the direct integration of PSCs with a planarized CFRP composite substrate. We show that the successful integration of devices onto the surface of the CFRP necessitates the planarization of the substrate, together with the use of a crack-prevention layer that is formed from a “wrinkled”  $\text{SiO}_2$  film that is formed onto the surface of the planarization layer. This wrinkled structure is created by partially softening the surface of the primer and planarization layer as a result of the thermal energy provided by the e-beam deposition process. This wrinkling likely enhances the bonding of the ITO electrode to the surface, and prevents the long-range propagation of cracks that would otherwise result in short-circuit devices. The PSC devices fabricated employ transparent bottom and top ITO contacts, which impart an enhanced degree of stability to the device. The devices fabricated had a stabilized PCE of 14.5%; a value that

compares favorably with control devices fabricated onto conventional ITO/glass substrates. The devices realized had a specific power (power per mass) of  $21.4 \text{ W g}^{-1}$  (an estimate that ignores the mass of the CFRP substrate), with the practical application of this technology requiring the development of ultralow mass encapsulation layers. The substrates utilized combine high strength and low mass, making them directly applicable as structural materials that can simultaneously generate electrical power. We expect further work (including device deposition by spray-coating, device scale-up, modularization and encapsulation) to create systems having direct employment in mobile power applications, including UAVs, HAPSSs, and electric vehicles.

#### Supporting Information

Supporting Information is available from the Wiley Online Library or from the author.

#### Acknowledgements

O.S.G., T.T. and F.C.M. contributed equally to this work. This work was funded by the Engineering and Physical Sciences Research Council (EPSRC) grant EP/S009213/1 (The Integration of Photovoltaic Devices with Carbon-Fiber Composites). E.J.C. thanks the EPSRC for a PhD studentship from grant EP/L01551X/1 (Centre for Doctoral Training in New and Sustainable PV). R.H.G. thanks the EPSRC for a PhD studentship from grant EP/T012455/1 (Molecular Photonic Breadboards). T.T. thanks the University of Sheffield for the provision of a PhD studentship.

#### Conflict of Interest

D.G.L. is a co-director of the company Ossila Ltd. which retails materials and equipment used in perovskite photovoltaic device research and development.

#### Data Availability Statement

The data that support the findings of this study are available from the corresponding author upon reasonable request.

#### Keywords

carbon-fiber-reinforced polymers, integrated photovoltaics, perovskite solar cells, specific power, structural photovoltaics

Received: October 27, 2022

Revised: March 7, 2023

Published online:

- [1] NREL, NREL Best Research-Cell Efficiency Chart, <https://www.nrel.gov/pv/cell-efficiency.html>, (accessed 25 October 2022).
- [2] W. Zhang, G. E. Eperon, H. J. Snaith, *Nat. Energy* **2016**, *1*, 16048.
- [3] S. Kim, H. Oh, G. Kang, I. K. Han, I. Jeong, M. Park, *ACS Appl. Energy Mater.* **2020**, *3*, 6995.
- [4] F. Di Giacomo, A. Fakharuddin, R. Jose, T. M. Brown, *Energy Environ. Sci.* **2016**, *9*, 3007.

- [5] P. Li, Z. Wu, H. Hu, Y. Zhang, T. Xiao, X. Lu, Z. Ren, G. Li, Z. Wu, J. Hao, H. L. Zhang, Z. Zheng, *ACS Appl. Mater. Interfaces* **2020**, *12*, 26050.
- [6] G. S. Han, S. Lee, M. L. Duff, F. Qin, J. K. Lee, *ACS Appl. Mater. Interfaces* **2018**, *10*, 4697.
- [7] J. Troughton, D. Bryant, K. Wojciechowski, M. J. Carnie, H. Snaith, D. A. Worsley, T. M. Watson, *J. Mater. Chem. A* **2015**, *3*, 9141.
- [8] B. Abdollahi Nejand, P. Nazari, S. Gharibzadeh, V. Ahmadi, A. Moshaii, *Chem. Commun.* **2017**, *53*, 747.
- [9] J. H. Heo, D. H. Shin, M. L. Lee, M. G. Kang, S. H. Im, *ACS Appl. Mater. Interfaces* **2018**, *10*, 31413.
- [10] B. T. Feleki, S. Chandrashekar, R. K. M. Bouwer, M. M. Wienk, R. A. J. Janssen, *Sol. RRL* **2020**, *4*, 2000385.
- [11] Z. Zhang, X. Li, G. Guan, S. Pan, Z. Zhu, D. Ren, H. Peng, *Angew. Chem., Int. Ed.* **2014**, *53*, 11571.
- [12] B. Dong, J. Hu, X. Xiao, S. Tang, X. Gao, Z. Peng, D. Zou, *Adv. Mater. Technol.* **2019**, *4*, 1900131.
- [13] M. Peng, B. Dong, D. Zou, *J Energy Chem* **2018**, *27*, 611.
- [14] R. Li, X. Xiang, X. Tong, J. Zou, Q. Li, *Adv. Mater.* **2015**, *27*, 3831.
- [15] L. Gao, L. Chao, M. Hou, J. Liang, Y. Chen, H.-D. Yu, W. Huang, *Npj Flex Electron* **2019**, *3*, 4.
- [16] S. Castro-Hermosa, J. Dagar, A. Marsella, T. M. Brown, *IEEE Electron Device Lett.* **2017**, *38*, 1278.
- [17] W. Zhai, Z. Zhu, X. Sun, H. Peng, *Adv. Fiber Mater.* **2022**, *4*, 1293.
- [18] Q. Wali, F. J. Iftikhar, N. K. Elumalai, Y. Iqbal, S. Yousaf, S. Iqbal, R. Jose, *Curr. Appl. Phys.* **2020**, *20*, 720.
- [19] W. Zeng, L. Shu, Q. Li, S. Chen, F. Wang, X.-M. Tao, *Adv. Mater.* **2014**, *26*, 5310.
- [20] F. Brunetti, A. Operamolla, S. Castro-Hermosa, G. Lucarelli, V. Manca, G. M. Farinola, T. M. Brown, *Adv. Funct. Mater.* **2019**, *29*, 1806798.
- [21] M. Kaltenbrunner, G. Adam, E. D. Głowacki, M. Drack, R. Schwödau, L. Leonat, D. H. Apaydin, H. Groiss, M. C. Scharber, M. S. White, N. S. Sariciftci, S. Bauer, *Nat. Mater.* **2015**, *14*, 1032.
- [22] S. Kang, J. Jeong, S. Cho, Y. J. Yoon, S. Park, S. Lim, J. Y. Kim, H. Ko, *J. Mater. Chem. A* **2019**, *7*, 1107.
- [23] J. Wu, P. Chen, H. Xu, M. Yu, L. Li, H. Yan, Y. Huangfu, Y. Xiao, X. Yang, L. Zhao, W. Wang, Q. Gong, R. Zhu, *Sci. China Mater.* **2022**, *65*, 2319.
- [24] Y.-K. Lee, Z. Xi, Y.-J. Lee, Y.-H. Kim, Y. Hao, H. Choi, M.-G. Lee, Y.-C. Joo, C. Kim, J.-M. Lien, I.-S. Choi, *Sci. Adv.* **2020**, *6*, 6212.
- [25] G. Lee, M. Kim, Y. W. Choi, N. Ahn, J. Jang, J. Yoon, S. M. Kim, J. Lee, D. Kang, H. S. Jung, M. Choi, *Energy Environ. Sci.* **2019**, *12*, 3182.
- [26] H. Xie, X. Yin, Y. Guo, J. Liu, W. Que, G. Wang, *Phys. Status Solidi RRL* **2019**, *13*, 1800566.
- [27] P. Mallick, *Fiber reinforced composites*, Elsevier, **2017**, Vol. 20072757.
- [28] G. D. Goh, Y. L. Yap, S. Agarwala, W. Y. Yeong, *Adv. Mater. Technol.* **2019**, *4*, 1800271.
- [29] T. Thornber, O. S. Game, E. J. Cassella, M. E. O'Kane, J. E. Bishop, T. J. Routledge, T. I. Alanazi, M. Togay, P. J. M. Isherwood, L. C. Infante-Ortega, D. B. Hammond, J. M. Walls, D. G. Lidzey, *ACS Appl. Mater. Interfaces* **2022**, *14*, 37587.
- [30] J. Gonzalo, D. López, D. Domínguez, A. García, A. Escapa, *Prog. Aerosp. Sci.* **2018**, *98*, 37.
- [31] J. Hur, K. Im, U. J. Kim, T.-H. Kim, J.-J. Park, S. Hwang, N. Park, *Jpn. J. Appl. Phys.* **2014**, *53*, 05HB01.
- [32] V. Zardetto, G. Mincuzzi, F. De Rossi, F. Di Giacomo, A. Reale, A. Di Carlo, T. M. Brown, *Appl. Energy* **2014**, *113*, 1155.
- [33] W. F. Wu, B. S. Chiou, *Thin Solid Films* **1997**, *293*, 244.
- [34] C. Wang, H. Zhang, F. Yang, Y. Fan, Q. Liu, *RSC Adv.* **2017**, *7*, 25483.
- [35] C. C. Shih, W. Y. Lee, C. Lu, H. C. Wu, W. C. Chen, *Adv. Electron. Mater.* **2017**, *3*, 1600477.
- [36] N. Bowden, B. Brittain, A. G. Evans, J. W. Hutchinson, G. M. Whitesides, *Nature* **1998**, *393*, 146.
- [37] W. H. Koo, S. M. Jeong, F. Araoka, K. Ishikawa, S. Nishimura, T. Toyooka, H. Takezoe, *Nat. Photonics.* **2010**, *4*, 222.
- [38] R. R. Seghi, J. A. Sorenson, *Int. J. Prosthodontics* **1995**, *8*, 239.
- [39] D. Guldiren, I. Erdem, S. Aydin, *J. Non-Cryst. Solids* **2016**, *441*, 1.
- [40] J. A. Smith, O. S. Game, J. E. Bishop, E. L. K. Spooner, R. C. Kilbride, C. Greenland, R. Jayaprakash, T. I. Alanazi, E. J. Cassella, A. Tejada, G. Chistiakova, M. Wong-Stringer, T. J. Routledge, A. J. Parnell, D. B. Hammond, D. G. Lidzey, *ACS Appl. Energy Mater.* **2020**, *3*, 5552.
- [41] J. E. Bishop, C. D. Read, J. A. Smith, T. J. Routledge, D. G. Lidzey, *Sci. Rep.* **2020**, *10*, 6610.
- [42] A. J. Bett, K. M. Winkler, M. Bivour, L. Cojocar, Ö. Ş. Kabakli, P. S. C. Schulze, G. Siefert, L. Tutsch, M. Hermle, S. W. Glunz, J. C. Goldschmidt, *ACS Appl. Mater. Interfaces* **2019**, *11*, 45796.
- [43] A. K. Jena, A. Kulkarni, T. Miyasaka, *Chem. Rev.* **2019**, *119*, 3036.
- [44] N. J. Jeon, H. Na, E. H. J., T. Y. Yang, Y. G. Lee, G. Kim, H. W. Shin, S. I. Seok, J. Lee, J. Seo, *Nat. Energy* **2018**, *3*, 682.
- [45] M. V. Khenkin, E. A. Katz, A. Abate, G. Bardizza, J. J. Berry, C. Brabec, F. Brunetti, V. Bulović, Q. Burlingame, A. Di Carlo, R. Cheacharoen, Y. B. Cheng, A. Colmann, S. Cros, K. Domanski, M. Dusza, C. J. Fell, S. R. Forrest, Y. Galagan, D. Di Girolamo, M. Grätzel, A. Hagfeldt, E. von Hauff, H. Hoppe, J. Kettle, H. Köbler, M. S. Leite, S. Liu, Y. L. Loo, et al., *Nat. Energy* **2020**, *5*, 35.
- [46] M. Saliba, T. Matsui, J. Seo, K. Domanski, J. Correa-Baena, M. K. Nazeeruddin, S. M. Zakeeruddin, W. Tress, A. Abate, A. Hagfeldt, M. Grätzel, *Energy Environ. Sci.* **2016**, *9*, 1989.
- [47] Y. Kato, L. K. Ono, M. V. Lee, S. Wang, S. R. Raga, Y. Qi, *Adv. Mater. Interfaces* **2015**, *2*, 1500195.
- [48] S. Svanström, T. J. Jacobsson, G. Boschloo, E. M. J. Johansson, H. Rensmo, U. B. Cappel, *ACS Appl. Mater. Interfaces* **2020**, *12*, 7212.
- [49] L. Zhao, R. A. Kerner, Z. Xiao, Y. L. Lin, K. M. Lee, J. Schwartz, B. P. Rand, *ACS Energy Lett.* **2016**, *1*, 595.
- [50] X. Zhang, C. Zhang, D. Li, S. Cao, M. Yin, P. Wang, G. Ding, L. Yang, J. Cheng, L. Lu, *Nanoscale Res. Lett.* **2019**, *14*, 324.
- [51] R. M. Barrer, G. Skirrow, *J. Polym. Sci.* **1948**, *3*, 549.